Classification of Lymph Node Tumor Images Using Adaptive Filtering in Convolutional Neural Networks

Jamal M. Alothman[1], Nameer N. El. Emam[2], Issa Qabajeh[3]*, Mhammed Almakadmeh[4]
Computer Science Department-College of Information Technology, Amman Arab University, Jordan[1, 2]
Software Engineering Department-College of Information Technology, Amman Arab University, Jordan[3]
École de Technologie Supérieure, Université du Québec, Montréal, Canada[4]

***Abstract*—Tumors of the lymphatic system can be either benign or malignant. However, because traditional diagnostic approaches rely on subjective assessment by individual pathologists and often lead to significant discrepancies and misclassifications, early and accurate diagnosis is important for successful treatment and improved scientific outcomes. We compare an adaptive convolutional neural network (CNN) model, trained on filter shapes, with regular CNNs by benchmarking them for image classification. This adaptive model automatically retunes filter size based on statistical tests of images, improving feature extraction and classification performance. More specifically, it achieves an accuracy of around 92%, which is about 10- 13% higher than random predictions using most standard models; however, it also has high precision and recall, 94% and approximately 4.5% higher in this metric, and 85%, with a further 27% increase relative to standard benchmarks used for others. An F1-score of 89% represents an 18% uplift, while AUC, at 97, outperforms the same model without ours by up to 11%. In addition, the mean squared error (MSE) is reduced to 0.096 for the adaptive model, compared with 0.24 for traditional methods. The results show that an adaptive filter can benefit CNN-based image classification. This exploratory research opens a new opportunity to apply deep learning methodologies in practice, supporting their integration into real-world applications such as medical imaging, autonomous systems, and security analysis. Although a small step, it shows the model as an efficient, fast, and scalable classification solution.**

Keywords*—Convolutional neural networks; adaptive image filtering; lymph node tumor images; image classification; feature extraction

I. Introduction

Tumor image classification from lymph nodes is becoming a major part of clinical practice across fields, especially in specialties such as oncology, where distinguishing malignant lymph node data has an enormous impact on patient decision-making and treatment [1]. Deep learning methods, particularly convolutional neural networks (CNNs), have propelled the day-to-day practice of classifying medical images, even those with non-rigid shapes or structures, with surprising accuracy. CNNs detect lesions, and other image types, such as chest X-rays, are classified for many diseases, alongside ultrasound, mammogram, and CT images [2],[3]. Additionally, recent use of established tools such as deep neural networks and wavelet transform models captures natural phenomena that increase representational power through intuitive feature engineering, with less complexity, to classify evolved images in a computationally efficient way [4].

*Corresponding author.

One major issue in tumor classification of lymph nodes is its strong dependence on subtle image variability used to distinguish malignant from benign nodes. To address this limitation, several authors have proposed modifications to standard CNN architectures, focusing on spatial information fusion and multi-task learning to improve lymph node localization/imaging and classification [5],[3]. Lastly, optimizers such as the seagull optimization method have also been used to fine-tune CNN parameters and improve their performance on other datasets [6].

In this field, CNNs contribute to more than just lymph node detection. They also have broader applications in oncology, such as breast cancer classification [7] and histopathology image analysis. CNNs have been widely used to solve many difficult computer vision problems and achieve much higher precision and recall (thus justifying their role in clinical scenarios) [2]. Most impressively, engineering teams have paired the two technologies. They have combined convolutional neural networks (CNNs) with various diagnostic modalities, including axial PET/CT images. This method is relatively simple, but assists in deciding whether it is metastatic lymph nodes or lymphoma. Therefore, their use in these treatments is justified, as they are part of personalized medicine [8].

Nevertheless, the challenges presented by medical imaging and similar features between malignant and nonmalignant tissues maintain significant barriers to accurate lymphoma classification. As a result, most deep learning architectures are based on convolutional neural networks. Nonetheless, most of these architectures have limited ability to capture complex, embedded spatial relationships and long-range dependencies in medical images [9]. Moreover, with other available imaging modalities and sufficient features to extract from different perspectives, classification becomes a daunting task. In this context, the recently leveraged neural network graphs are heterogeneous graph convolutional networks (HGCNs) that facilitate multi-view data integration, thereby increasing the informational content of complex medical datasets [4].

Convolutional neural network training is based on a linear combination of properly chosen convolutional filters in CNNs to improve image classification. The study explores feature discovery, computational efficiency, and classification accuracy to understand and quantify the impact of changes to CNN designs on model performance. This will be further optimized into a CNN architecture for better image classification. Finally, the practical guidelines reviewed in the study could inform a new direction for adaptive CNN filter selection.

With the rapid development of image processing and optimization techniques, convolutional neural network-based methods for classifying lymph node tumors from histopathological images are practical and hold great promise in medical imaging. These advances will profoundly affect diagnostic accuracy and clinical efficiency while minimizing misdiagnoses and improving patient outcomes [10],[11].

II. Related Work

An adaptive image filter selection method has substantially improved the automatic classification of lymph node tumors using convolutional neural networks, thereby enhancing accuracy and efficiency. Previous studies in this area have explored several strengths and limitations, with some following alternative imaging techniques and practices.

Cadillo-Laurentt and Paiva-Peredo compiled a dataset of breast cancer lymph nodes and applied a convolutional neural network to classify histopathological images. The results provided a strong framework for applying convolutional neural networks to lymph node studies and introduced DenseNet architectures, thereby improving diagnostic performance [12]. Likewise, Wang et al. conducted a case study to classify malignant lymph nodes in patients with head and neck cancer. The study addresses one of the most immediate needs in malignancy detection in machine learning-based systems: the use of CT radiomics and a convolutional neural network (CNN) to improve the precision of malignant node identification for radiotherapy [4]. This is partly due to the training data up to October 2023, which demonstrates the usefulness of such models in medicine through their research.

Furthermore, Nayan et al. investigated the challenges of detecting and segmenting mediastinal lymph nodes and presented a modified UNet++ architecture adapted to image resolution and texture discontinuities [13]. Through this study, I learned how the same deep learning models can be tailored for medical imaging to improve image segmentation. Heinlein et al. also addressed lymph node metastasis detection in whole-slide images using a transformer-guided multiple-instance learning approach [14]. They addressed problems typical of standard convolutional neural networks, which can become restrictive when processing large images.

In addition, Ding et al. and Uthatham et al. are representative studies that examine novel network architectures and compare batch normalization in existing CNN models. Ding et al. proposed a convolutional network based on the wavelet transform to classify cervical lymph node metastasis, enhancing feature extraction through spatial and frequency-domain analyses [11]. Uthatham et al. compared several CNN architectures for lymph node classification and found DenseNet to be the optimal model [15].

Moreover, Huang et al. designed and trained a CNN on gigapixel images to identify lymph node metastasis, confirming that CNNs achieve high sensitivity and specificity across heterogeneous datasets [16]. Additionally, Cari et al. and Chao et al. studied modified CNN architectures and graph neural networks to identify lung cancer and gross tumor volume in lymph nodes, respectively, underscoring the importance of deep learning models in X-ray cancer imaging [17, 18].

The PatchCamelyon benchmark dataset, designed by Veeling et al. for classifying histopathology images using deep learning methods [19], was used to address the challenge of microscopic pathology images that differ in projection under arbitrary rotation. They proposed rotation-equivariant convolutional neural networks as a solution. Group-equivariant convolution layers ensured the same features were detected regardless of angle. They extended this architecture to the PCam dataset, achieving better tumor detection than regular convolutional neural networks because medical image classification systems require spatial invariance.

Jaiswal et al. noted that only a few studies use semi-supervised learning to detect lymph node metastases in histopathological images [20]. The researchers used convolutional neural network architectures, specifically DenseNet-based models, and a pseudo-labeling method to leverage both labeled and unlabeled samples during training. At test time, they used a simple framework that included several test-time augmentation methods to improve the system's ability to classify more samples correctly. They demonstrated that semi-supervised methods can leverage large portions of otherwise unused data through their work on the PatchCamelyon dataset.

Teh et al. investigated how limited annotated data constrains digital pathology research and developed a weakly supervised learning framework for patch classification [21]. The research team used transfer learning techniques with ProxyNCA metric learning methods to improve convolutional neural networks' ability to distinguish tumors from normal tissue. The researchers evaluated the method on the PatchCamelyon dataset and found that weakly labeled pretraining improved classification performance while reducing the need for extensive manual annotation.

Zhong et al. developed a cancer image classification approach based on the DenseNet architecture to improve the identification of metastatic tissue in lymph node images [22]. Their methodology employed deep convolutional neural networks, along with extensive data augmentation and test-time augmentation, to improve model generalization. The researchers showed that deep, densely connected networks can effectively perform histopathological image analysis by training and testing the DenseNet model on the PatchCamelyon dataset, yielding high classification accuracy.

Jin et al. provided a unified deep learning framework that integrates convolutional neural networks with U-Net segmentation information [23]. The authors introduced ConcatNet, which combines spatial bulk tumor-derived features from segmentation maps with image units derived from CNN processing. To demonstrate its value, they evaluated it on the PatchCamelyon dataset and found that segmentation data improves generalization by better distinguishing tumor patterns and classifying different tumors.

Teh and Taylor recently examined prevailing image resolutions in digital pathology and their corresponding performance on deep learning models [24]. The authors examined how input and image resolution affect classification accuracy in convolutional neural networks. They assessed different CNN architectures on the PatchCamelyon dataset and found that larger patches (2× 4× patch sizes) were required for histology analysis to achieve better classification performance, as correct decision-

making depends on identifying histopathological structural elements inherent in tissue. A partitioned multi-scale and multi-head self-attention ensemble network was introduced by Ge et al. Breast Cancer Pathology Patches [ML5] [25]. It uses multi-scale feature extraction and attention-based methods to better extract intricate histopathological structures. The researchers evaluated their model on the PatchCamelyon dataset and demonstrated that attention-based ensemble approaches dramatically enhance classification performance by strengthening local and global features in pathology images.

These investigations provide a solid foundation for using CNNs to classify tumors in lymph nodes. They improved the speed and accuracy of the diagnosis and enabled higher-order models that can cope with some aspects of the complexity inherent in medical imaging data. The future emergence of these methodologies is also likely to improve cancer patient management more precisely and effectively.

III. Research Design and Analysis

The methodology describes the research design for developing and testing an adaptive CNN for tumor classification in lymph nodes. The experiment was conducted on the PatchCamelyon dataset with proper preprocessing.

A standard CNN approach takes a pre-processed image dataset as input, represented by each image in Fig. 1. Each image selected in the previous step passes through multiple convolutional layers, using learnable filters and activation functions/more max-pooling operations, to extract features. They are flattened and sent to a pair of fully connected layers, the classifier, during training. This organizes the output processing through a complete pipeline, going from preprocessing/feature extraction to classification.

Many activation functions are critical components of a feed-forward neural network because they add non-linearities that allow a model to learn complex patterns (which no simple linear transformation can capture). Without these functions, every layer is linear, and stacking a number of layers removes any non-linearity from the model, making it really weak and ill-posed. In the same spirit, activation functions regulate information flow: they amplify relevant signals and attenuate uninformative ones. They affect the gradient flow during backpropagation, which is one of the factors that determine model learning stability and speed. Some functions help with solving issues such as vanishing or exploding gradients. Activation functions (ReLU) are used for speeding up training and reducing computation (fewer operations than sigmoid), Sigmoid: For binary output, tanh clusters outputs around zero, so that it's easier for us to train. In summary, activation functions enable deep learning models to learn complex real-world relationships internally and thus serve their purpose well by efficiently performing classification, detection, and pattern recognition tasks.

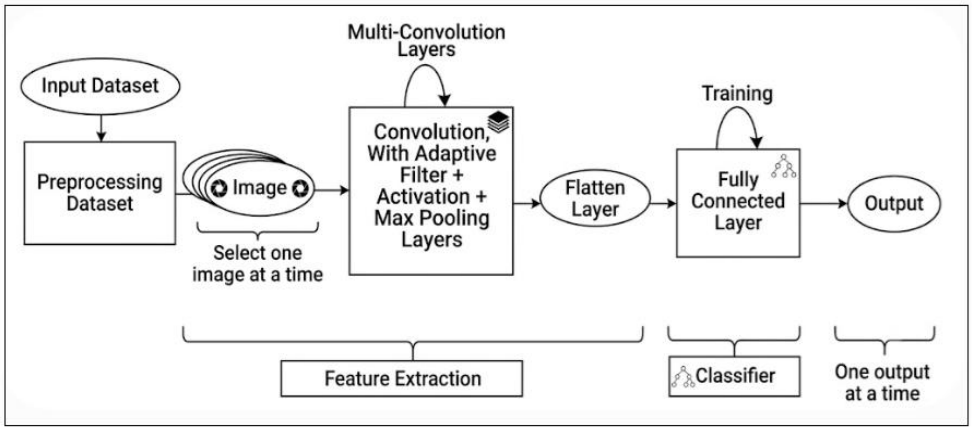

Fig. 1. The Proposed CNN workflow using adaptive filter selection.

A. Dataset Collection

The PCam is a large-scale histopathology dataset consisting of 327,680 color patches (96×96 pixels) extracted from whole-slide images of lymph node tissue [19]. It is intended to detect tumor spread. This binary label indicates the presence of metastatic cancer cells in each patch, making it a relevant and manageable benchmark for machine learning. Based on the CAMELYON16 challenge, this dataset has an even split of training/validation/test sets to ensure reliable experimentation in medical image classification. PCam is favored because, although some metastasis detection tasks are complex, image recognition is practically trivial for the machine, given its ability to train on a single GPU. Data collection is the first step in image classification and can be sourced from public repositories or produced as needed for a specific research purpose. From existing public databases or developed with the same aims of research, without a comprehensive dataset made prior to classification. This study uses primary datasets. The PCam benchmark is original and, at the same time, very challenging. It gained popularity due to its strong fit for medical imaging applications.

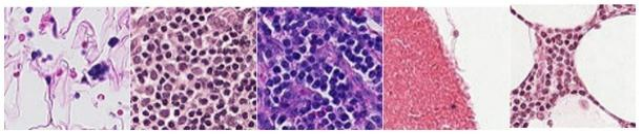

Fig. 2. PatchCamelyon dataset sample images.

Fig. 2 displays sample images from the PatchCamelyon dataset. These images represent the input data used in the preprocessing and feature extraction pipeline described in Algorithmic framework-1.

Algorithmic framework-1: Preprocessing

Step 1: Load PatchCamelyon dataset D_{raw} that includes two attributes (i^{th} image x_i with the corresponding binary i^{th} image label y_i) as in Eq. (1):

$$L_{D_{raw}} = \{(x_i, y_i)\}_{i=1}^{N} \quad (1)$$

where:

$$y_i \in \{0,1\} \text{ is } i^{th} \text{ image label}$$

Such that $y_i =$

$$\begin{cases} 0, & if\ xi\ is\ normal\ tissue \\ 1, & if\ xi\ is\ tumor\ tissue \end{cases} \quad (2)$$

is the number of images

Step 2: Splitting data D_{raw} into three sections {training 70%, validation 15%, and testing 15%} as shown in Eq. (3).

$$D_{raw} = D_{train} \bigcup D_{val} \bigcup D_{test} \quad (3)$$

Step 3: Load a set of Images ($L_{\hat{D}}(x_i)$) from the dataset $\hat{D}$ for each image index x_i shown in Step 1, see Eq. (4):

$$L_{\hat{D}}(i) = \hat{D} = \{(\hat{x}_i, y_i)\}_{i=1}^{N} \quad (4)$$

where $\hat{x}_i$ is the image at the index i. Thus, the loaded dataset becomes:

Step 4: Verify Label Alignment by checking each image-label pair to ensure that every image matches its correct annotation, as in Eq. (5) and (6).

$$A(\hat{x}_i, y_i) = \begin{cases} 1, & if\ the\ image\ matches\ its\ correct\ label \\ 0, & otherwise \end{cases} \quad (5)$$

Keep only correctly aligned pairs as in Eq. (7):

$$D_{aligned} = \{(\hat{x}_i, y_i) \in \hat{D} \mid A(\hat{x}_i, y_i) = 1\}$$

Step 5: Validate Image Dimensions:

Step 5.1: Verify that all images meet the required spatial resolution of (96 × 96 × 3 pixels (RGB) standard.

Step 5.2: Define the dimension function $dim(\hat{x}_i)$ *as in* Eq. (7):

$$dim(\hat{x}_i) = (h_i \times w_i \times c_i), where\ h_i = 96, w_i = 96, and\ c_i = 3 \quad (7)$$

Step 6: Apply Color Normalization using the Macenko method [26]. //*This method is important for Histopathology to reduce variability due to different staining protocols.*

Step 7: Check Class Distribution**:** Show a trustworthy distribution that balances tumor and normal image samples throughout the collection; see Eq. (8) and (9).

$$N0 = \sum_{i=1}^{\hat{D}} I(y_i = 0) \quad (8)$$

$$N1 = \sum_{i=1}^{|\hat{D}|} \mathbb{I}(y_i = 1) \quad (9)$$

where $\mathrm{I}(\cdot)$ is the indicator function, and the class distribution and the probability of each class are defined in Eq. (10) and (11)

$$P(y = 0) = \frac{N_0}{|\hat{D}|} \quad (10)$$

$$P(y = 1) = \frac{N_1}{|\hat{D}|} \quad (11)$$

Step 8: Finalize the Preprocessed Dataset:

Create a complete, verified dataset structure (D_{final}) to train the Adaptive convolutional neural network model.

B. The Proposed Adaptive Convolutional Neural Networks (ACNN) Algorithm

In the CNN architecture, tasks such as preprocessing and layers that are closely related to each other, for example, Conv2D, MaxPooling2D, Flatten, and Dense, are instantiated together. A Conv2D layer applies 2D convolution to extract spatial features, and with the help of MaxPooling2D layers, your model can train faster and is less prone to overfitting, as they reduce the number of pixels while preserving their values. A Flatten layer transforms multidimensional feature maps into a one-dimensional vector to feed to the next Dense (fully connected) layer, which performs classification/regression on these features. Proper preprocessing at every level creates high-quality input data, which helps assist the model and achieve higher performance. As shown in Fig. 3, the CNN architecture for image classification is proposed.

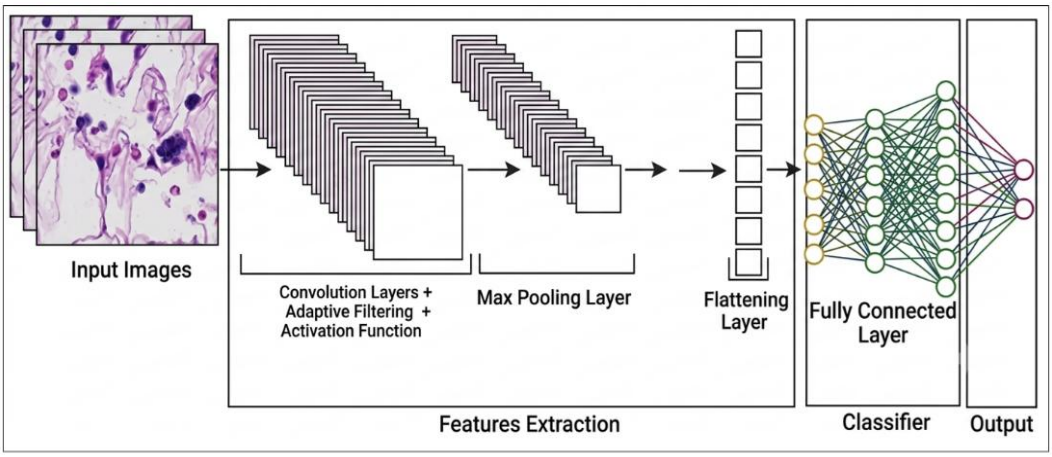

Fig. 3. CNN architecture model for image classification $Conv_{64\times5\times5\times3}$.

Adaptive Convolutional Neural Networks (ACNNs) will adjust their functions and architectures based on the information and task demands, enabling better performance across different tasks and conditions (without pre-training or retraining the network). Algorithmic framework-2 is the proposed framework that follows a pipeline depending on the dataset using ACNN. It starts by selecting images and preprocessing the PatchCamelyon dataset, and then adapts to compute pixel variance-based statistical measures for filtering; see Eq. (1)-(3). For each image, the method selects a convolution size (64 filters, 5×5, or 32 filters, 3×3), applies ReLU activation, and performs max pooling for all operations (Table I). The final classifier consists of a fully connected layer, a flattening layer, and a softmax layer to produce the final outputs.

Algorithmic framework-2: The Proposed ACNN

Step 1: Select a dataset (DS = PatchCamelyon) that includes N images;

Step 2: Read images $I_i \quad \forall i = 1, \dots, N$

Step 3: Define the image size $(Size_{I_{i,}} = n \times n \times 3)$; *// where n=96 using 3-channels (B)*

Step 4: Calculate the variance $(\delta_{I_i}^2)$ of I_i using Eq. (12), (13);

$$\delta_{I_i}^2 = \frac{1}{n \times n \times 3} \sum_{j=1}^{n \times n \times 3} \left(X_j - \mu_{I_i}\right)^2 \quad \forall i = 1, \dots, N \qquad (12)$$

$$\mu_{I_i} = \frac{1}{n \times n \times 3} \sum_{j=1}^{n \times n \times 3} X_j \qquad (13)$$

where:

X_j is the value of the j^{th} pixel in the image.

μ_{I_i} is the mean value of all pixels in the image I_i.

Step 5: Calculate the average variance of all images in DS (δ_{DS}^2) using Eq. (14).

$$\delta_{DS}^2 = \frac{1}{N} \sum_{i=1}^{N} \delta_{I_i}^2 \qquad (14)$$

Step 6: Set Stride =2;

Step 7: for *i = 1 to N // where i is the image index*

Step 7.1: If $(\delta_{I_i}^2 > \delta_{DS}^2)$ then

Apply convolution $Conv_{64\times5\times5\times3}$ using 64 filters, the $MaskSize = 5 \times 5 \times 3$ and the Stride=2;

Else

Apply convolution $Conv_{64\times3\times3\times3}$ using 64 filters, the $MaskSize = 3 \times 3 \times 3$ and the Stride=2;

Step 7.2: Calculate the new size of I_i^{Conv} $\left(NewSize_{I_i^{Conv}}\right)$ after the convolution process using Eq. (15)

$$NewSize_{I_i^{Conv}} = \left\lfloor \frac{\frac{Size_{I_{i,}}}{\sqrt{Size_{I_{i,}}}} - \frac{MaskSize}{\sqrt{Size_{I_{i,}}}}}{Stride} \right\rfloor + 1 \qquad (15)$$

Step 7.3: Update the $Size_{I_{i,}}$, see Eq. (16):

$$Size_{I_{i,}} = \left(NewSize_{I_i^{Conv}}\right)^2 \times 3 \qquad (16)$$

Step 7.4: Apply activation using the ReLU function $f(x)$ using Eq. (17);

$$f(x) = \max(0, x) \qquad (17)$$

Step 7.5: Apply Max Pooling with Stride =2, using Eq. (18);

$$I_{i,max,k}^{Conv} = max_{s=1}^{MaskSize}\ max_{r=1}^{MaskSize}\left(I_{i,s,r}^{Conv}\right),\ \forall k \qquad (18)$$

where

k- is the mask index in the image I_i^{Conv}.

Step 7.6: If flatten is reached with the length f then

Step 7.6.1: Apply fully connected neural networks of dense Layers using Eq. (19).

$$z_j^{[i]} = \sum_{l=1}^{ni-1} W_{j,l}^{[i]}\ a_l^{[i-1]} + b_j^{[i]} \qquad (19)$$

where:

$z_j^{[i]}$ is the linear activation for neuron j in layer i

$b_j^{[i]}$ is the bias for this particular neuron j.

$\sum_{l=1}^{ni-1}$ is the sum of inputs coming from the previous layer i−1.

$W_{j,l}^{[i]}$ is the weight of the connection between neuron l in layer i−1 and neuron j in

$a_l^{[i]}$ is the ReLU activation function

Step 7.6.2: Apply activation function between layers based on ReLU.

Else

Step 7.6.1: Calculate the variance ($\delta^2_{I_{i,max}^{Conv}}$) of $I_{i,max}^{Conv}$ using Eq. (20), (21);

$$\delta^2_{I_{i,max}^{Conv}} = \frac{1}{n \times n \times 3} \sum_{j=1}^{n \times n \times 3} \left(X_j - \mu_{i,max}^{Conv}\right)^2 \quad \forall i = 1, \dots, N \qquad (20)$$

$$\mu_{i,max}^{Conv} = \frac{1}{n \times n \times 3} \sum_{j=1}^{n \times n \times 3} X_j \qquad (21)$$

Step 7.7: Apply Softmax to build the classifier using Eq. (22);

$$Softmax(z)_i = \frac{e^{z_i}}{\sum_{j=1}^{f} e^{z_j}} \qquad (22)$$

where:

$(z)_i$ is the vector of i^{th} class of raw output from the neural network

e: Euler's number, the base of the natural logarithm = 2.718.

Step 8: End of For i

Step 9: End.

TABLE I. THE RANGE OF PARAMETERS USED IN THE PROPOSED MODEL

Parameters	Value/Condition
Batch size	128
Learning rate	0.001
Epochs	10
Filter size	5×5 or 3×3
Number of filters	64 or 32, based on adaptive condition (see ACNN Algorithm)
Loss function	Categorical Cross-Entropy
Optimizer	Adam
Number of convolution blocks	3
Convolution Block Contains	Conv2D + Activation function + Pooling
Activation function	ReLU
Pooling function	Max Pooling 2D 2 × 2
Hidden layers dimension	Dense1 (Size=128) + Dense2 (Size=64)
Output Layer	Softmax (Size=2)

A key aspect of our model design is implementing adaptive filtering that adjusts the filter size and parameters on the fly based on the input data's statistical properties. This approach shows great potential in aiding the network to learn more complex spatial relations and hierarchical features, which are important for improving accuracy in both feature extraction and classification tasks. Adaptive filtering is constructive in CNNs, as it changes how features are extracted based on input variability, as well as how local and global features are represented. In addition, it provides a spatial representation while reducing computational redundancy; thus, it forms the basis of sophisticated convolutional network architectures for applications such as medical imaging and object detection.

IV. RESULTS AND DISCUSSION

In this section, we provide a detailed analysis and discussion of the experimental results for image classification using the standard Convolutional Neural Network (CNN) model and the novel Adaptive Convolutional Neural Network (ACNN). Its main purpose is to study the ability of adaptive filtering methods to enhance classification performance. This section presents evaluation metrics, comparative experimental results with ROC analysis and confusion matrix interpretation, and a complete performance comparison.

A. Evaluation Metrics

To evaluate the proposed models' classification performance, we use several widely used metrics.

- True Positives (TP): Correctly predicted positive samples.
- True Negatives (TN): Correctly predicted negative samples.
- False Positives (FP): Negative samples incorrectly classified as positive.
- False Negatives (FN): Positive samples incorrectly classified as negative.

1) Accuracy: Accuracy measures the overall correctness of the model predictions [27] and is defined in Eq. (23):

$$\text{Accuracy} = \frac{TP+TN}{TP+TN+FP+FN} \tag{23}$$

This metric represents the ratio of correctly classified instances to the total number of predictions.

2) Precision: Precision evaluates the reliability of positive predictions made by the model [27], see Eq. (24):

$$\text{Precision} = \frac{TP}{TP+FP} \tag{24}$$

It is particularly important in scenarios where false positives carry significant consequences.

3) Recall: Recall (Sensitivity) measures the ability of the model to identify all actual positive instances [27], as in Eq. (25):

$$\text{Recall} = \frac{TP}{TP+FN} \tag{25}$$

High recall is crucial in medical applications, where missing positive cases can have severe consequences.

4) F1-Score: The F1-score is the harmonic mean of precision and recall [28], see Eq. (26):

$$\text{F1-Score} = 2 \times \frac{\text{Precision} \times \text{Recall}}{\text{Precision} + \text{Recall}} \tag{26}$$

It is particularly useful for imbalanced datasets.

5) Mean Squared Error (MSE): Mean Squared Error quantifies the average squared difference between predicted and actual values [27]:

Lower MSE values indicate better predictive performance and reduced error rates, see Eq. (27).

$$\text{MSE} = \frac{1}{n}\sum_{i=1}^{n} (y_i - \hat{y}_i)^2 \tag{27}$$

6) Confusion matrix: The confusion matrix provides a detailed breakdown of prediction outcomes, categorizing predictions into TP, TN, FP, and FN [28], as illustrated in Table II.

TABLE II. CONFUSION MATRIX

Total population = P + N		Predicted Condition	
		Positive	Negative
Actual Condition	Positive	True positive (TP)	False negative (FN)
	Negative	False positive (FP)	True negative (TN)

B. Performance Comparison of CNN Models

Case 1: Adaptive Model (32 or 16 Filters, 3×3)

The performance of the traditional CNN model with 32 filters and a 3×3 kernel over 10 training epochs is shown in Fig. 4. There are four main metrics monitored by the system: training accuracy, validation accuracy, training loss, and validation loss. They measure how well the model learns and generalizes to out-of-distribution data.

The training process shows continuous improvement, as shown in Fig. 4, with training accuracy reaching 94.66% by the final epoch. Training loss decreases continuously, reaching 14.20. Optimization is working, and predictions on the training data have improved. Validation accuracy increases, reaching a maximum of ~82.44%, indicating that the model generalizes relatively well to new data, though it remains lower than the training accuracy. The validation loss starts low and stays there through the middle epochs, then grows slightly and finally plateaus around 58.71, with only minor changes in generalization ability (less than one epoch). The gap between the training and validation metrics indicates typical CNN overfitting during training. This illustrates the model's effectiveness at learning relevant features, as training loss decreases and validation accuracy continues to increase.

Fig. 5 shows the training results for the adaptive CNN model, which uses 32 and 16 filters with a 3×3 kernel size over ten training epochs. The graph tracks training and validation accuracy and loss to evaluate how effectively the adaptive configuration learns and generalizes.

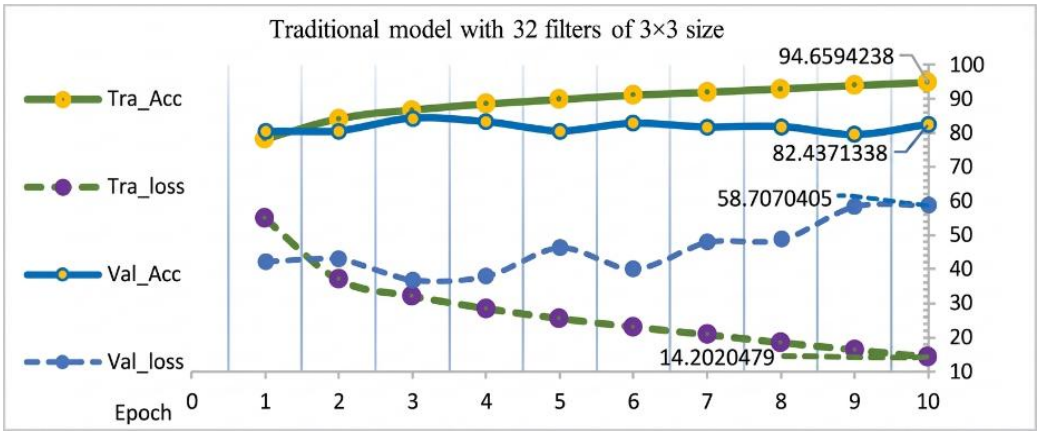

Fig. 4. Results for the traditional model with 32 filters of size 3×3.

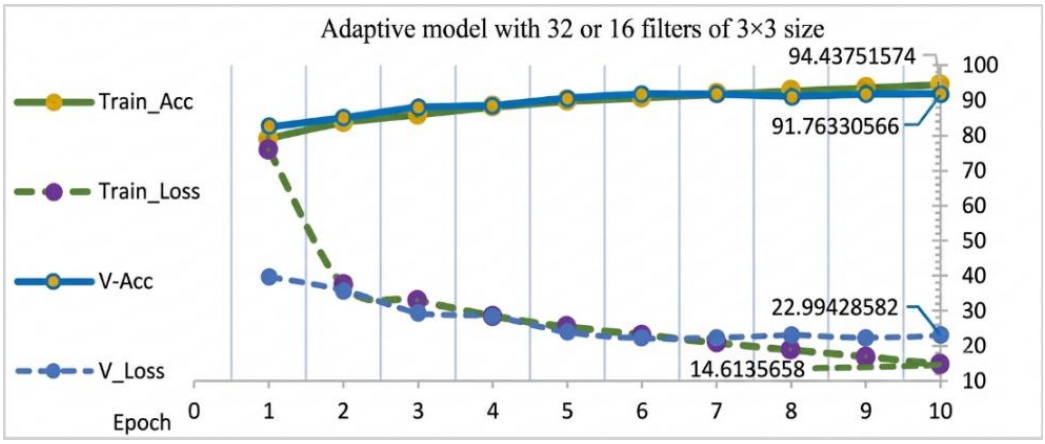

Fig. 5. Results for the adaptive model with 32 or 16 filters of size 3 ×3.

In Fig. 5, we observe a steady increase in model performance throughout training. Training accuracy increases steadily to about 94.44% by the last epoch, while training loss decreases rapidly and stabilizes around 14.61, indicating little error when the model is well trained. In addition, classic models generalize poorly, showing the largest increase in validation accuracy throughout training, to 91.76%. Validation loss decreases steadily to 22.99, with only slight variation across epochs. This improvement brings the adaptive model closer to the ideal case, where training and validation accuracies are close enough that generalization should be well under control. Stability is achieved because accuracy increases while loss decreases.

Case 2: Adaptive Model (64 or 32 Filters, 3×3)

Fig. 6 shows the training behavior of the traditional CNN model with 64 filters and a 3×3 kernel over 10 epochs. The curves show the progression of training and validation accuracy and loss, helping evaluate how well the model learns and generalizes.

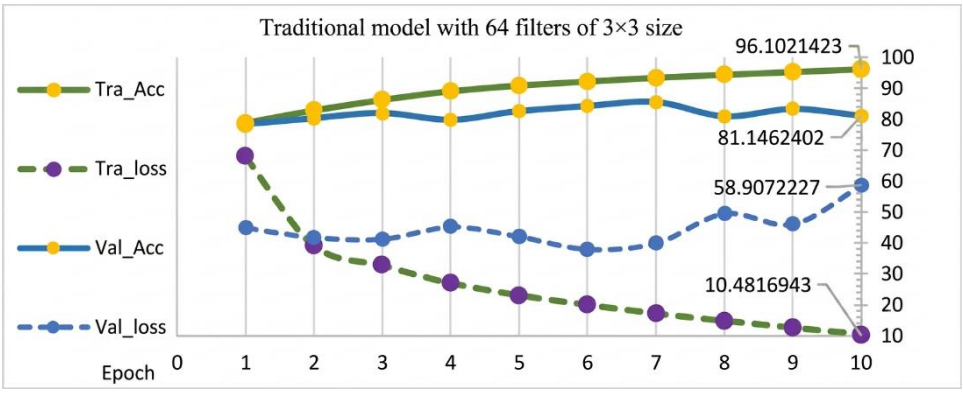

Fig. 6. Results for the traditional model with 64 filters of 3×3 size.

As shown in Fig. 6, the model continues to learn for most of the training period. Training accuracy continues to increase, reaching 96.10% at epoch = 175, while the training loss decreases to around 10.48, indicating that the model has been successfully optimized with fewer binary prediction errors. Validation accuracy reaches around 81.15%, with little change in later epochs. First, the validation loss decreases from its starting value, then increases, ending at 58.91, suggesting unstable generalization. The training and validation metrics differ significantly, indicating that the model has overfit the data. This suggests your model is learning important features from the dataset, as shown by the increase in accuracy and decrease in training loss.

The adaptive CNN model's performance on the training data is shown in Fig. 7, with 64 and 32 filters and a 3×3 kernel over 10 training periods. The plots will show how well the adaptive architecture learns (and generalizes) over time, as a function of training and validation accuracy, losses, and so forth.

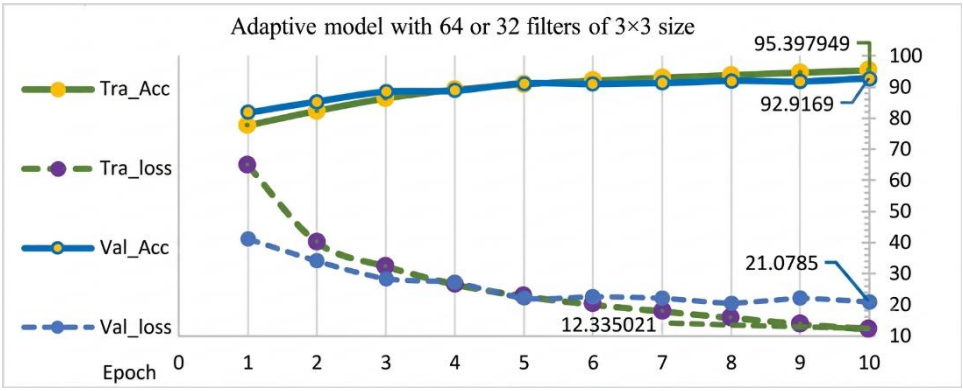

Fig. 7. Results for the adaptive model with 64 or 32 filters of size 3 × 3 size.

Fig. 7 shows that the learning process remains stable throughout the entire training period. Training accuracy increases, reaching about 95.40% at the end of training, while training loss drops to about 12.34, indicating that the model optimized the training data with fewer errors. Validation accuracy shows a similar upward trend, reaching about 92.92%, indicating strong generalization and close alignment with training performance. Validation loss decreases steadily, stabilizing at about 21.08, with only small variations during the middle training periods. The adaptive model achieves strong predictive performance because training and validation results stay close, as shown by the small difference between them. The adaptive configuration outperforms traditional configurations by improving accuracy while reducing loss.

C. Validation Accuracy Comparison

Fig. 8 presents a comparison of the validation accuracy between the traditional and adaptive CNN models over 10 training epochs. The comparison highlights the difference in performance and generalization capability between the two architectures during the validation phase.

Across all epochs (Fig. 8), the adaptive model's validation accuracy is higher than the traditional model's. For example, the adaptive model starts at 81.86% (compared to 78.31%) and steadily improves throughout training, whereas the traditional model learns more slowly. By the end of the last epoch, the adaptive model reaches around 92.92%, while the traditional model reaches ~81.15%, indicating a significant performance gap. The validation accuracies of the traditional (dotted) and adaptive (solid) models over 10 epochs. The traditional model's validation accuracy fluctuates significantly in the early epochs, whereas the adaptive model's steadily increases. This consistent performance indicates the adaptive architecture's ability to extract relevant features and generalize to unseen data.

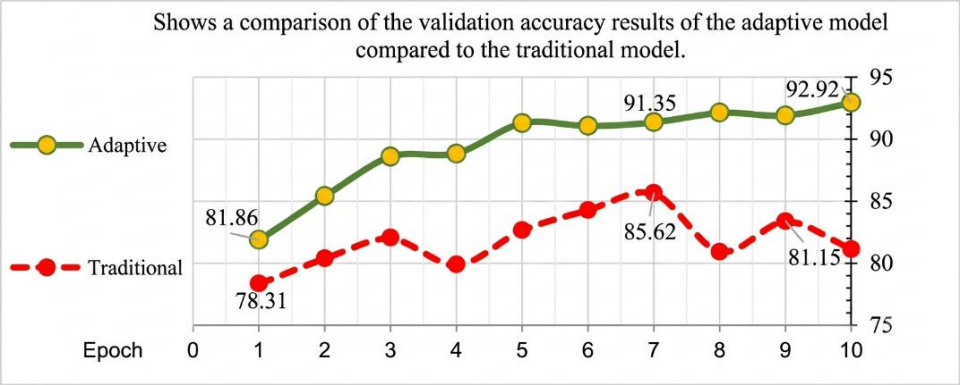

Fig. 8. Comparison of validation accuracy results for traditional models.

Overall, the comparison shows that the adaptive model achieves substantial improvements in validation performance and learning stability compared with the traditional model.

D. Validation Loss Comparison

As shown in Fig. 9, the adaptive model has produced lower validation loss across all epochs. By the end of the epoch, the adaptive CNN reached a validation loss of 0.2108, whereas the traditional model reached 0.5891 (overfitting).

The validation loss results clearly demonstrate that the adaptive model consistently outperforms the traditional model across all epochs. At the first epoch, the adaptive model starts with a validation loss of approximately 40, while the traditional model records about 43, indicating an initial improvement of 6.98%. As training progresses, the adaptive model steadily reduces its validation loss to 21.08 at epoch 10, while the traditional model's loss increases to 58.91. Using the final epoch values, the adaptive model achieves a 64.2% lower validation loss than the traditional model. Furthermore, comparing the adaptive model's own performance from the first to the last epoch, the validation loss decreases from approximately 40 to 21.08, representing a 47.3% improvement. These results indicate that the adaptive approach converges more effectively and remains more stable throughout training, leading to substantially better generalization than the traditional model.

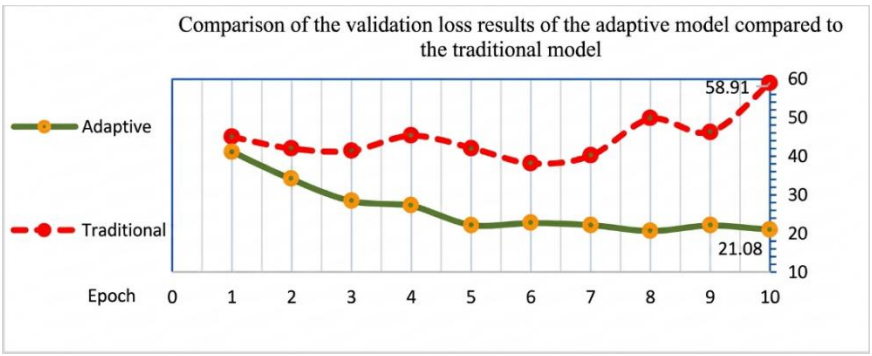

Fig. 9. Comparison of validation loss across traditional CNN models.

E. ROC Curve Analysis

ROC analysis further validated the adaptive model's superiority. The traditional CNN achieved an AUC of 0.86, while the adaptive CNN achieved an impressive 0.97 (Fig. 10 and 11).

A higher AUC indicates the adaptive model's enhanced ability to distinguish malignant from benign samples across all classification thresholds.

The ROC curve analysis shows that the adaptive model delivers substantially better classification performance than the traditional model. The traditional model achieved an Area Under the Curve (AUC) of 0.86, indicating good discrimination between classes, whereas the adaptive model achieved an AUC of 0.97, indicating excellent classification performance. The increase in AUC from 0.86 to 0.97 corresponds to an improvement of approximately 12.8%. In addition, the adaptive model's ROC curve is consistently closer to the upper-left corner, indicating a higher True Positive Rate (TPR) at lower False Positive Rates (FPR). This means the adaptive model can correctly identify more positive cases while producing fewer false alarms than the traditional model. At low FPR values, the adaptive model rapidly reaches TPR values above 0.85–0.90, whereas the traditional model requires considerably higher FPR values to attain comparable detection rates. When these ROC results are considered together with the validation loss analysis, the superiority of the adaptive model becomes even clearer. The adaptive model reduced the validation loss from approximately 40.0 to 21.08, while the traditional model ended with a validation loss of 58.91. Relative to the traditional model, the adaptive model achieved a 64.2% lower validation loss. Overall, the adaptive model demonstrates both higher predictive accuracy and better generalization capability. The 12.8% improvement in AUC and 64.2% reduction in validation loss confirm that the adaptive approach learns more effective decision boundaries, achieves su-

perior class discrimination, and maintains greater stability during training compared with the traditional model. These results indicate that the adaptive model is significantly more reliable and robust for practical deployment.

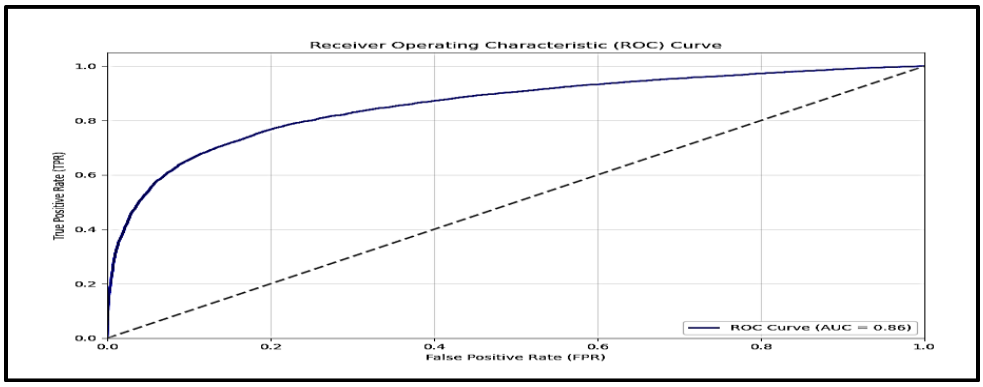

Fig. 10. ROC traditional model.

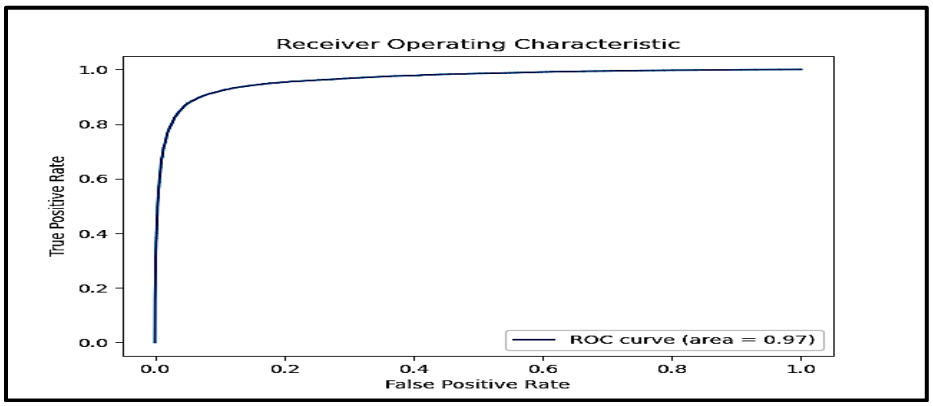

Fig. 11. ROC adaptive model.

F. Confusion Matrix Analysis

The confusion matrix of the old model (Fig.12) contains many false negatives (6,886) and false positives (1,012), making our recall on that not great.

On the contrary, as illustrated in Fig.13, using the adaptive model yields only 737 false positives and 2,429 false negatives, resulting in a significant reduction in misclassification and higher precision and recall. This adaptive filtering strategy proves to be a good choice for learning these potentially complex histopathological patterns.

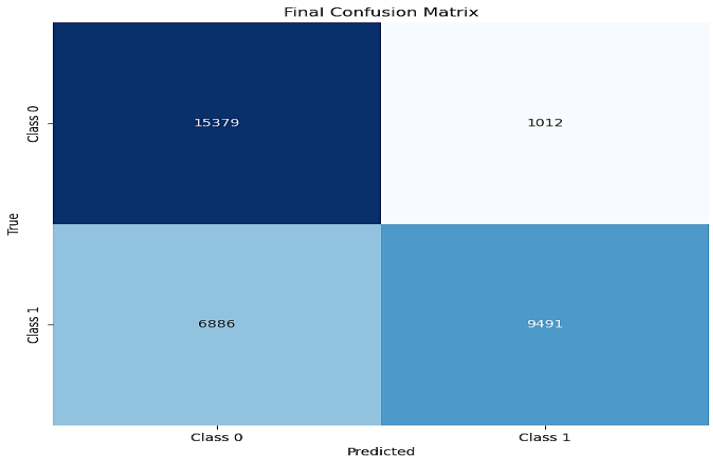

Fig. 12. Confusion matrix of the traditional filtering model using 64 × 3 × 3 filters.

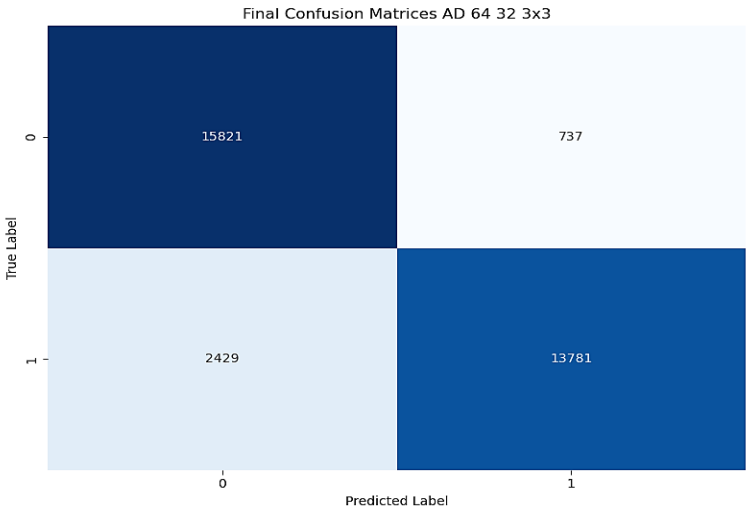

Fig. 13. Confusion matrix for the adaptive CNN model using 64 or 32 filters with a 3 × 3 kernel size.

The confusion matrix results indicate that the adaptive CNN model (64 or 32 filters, 3 × 3 kernel) performs substantially better than the traditional filtering model (64 × 3 × 3 filters). The traditional model correctly classified 15,379 Class 0 samples and 9,491 Class 1 samples, while misclassifying 1,012 false positives and 6,886 false negatives. In contrast, the adaptive model correctly classified 15,821 Class 0 samples and 13,781 Class 1 samples, with only 737 false positives and 2,429 false negatives. Based on these values, overall classification accuracy increased from 75.9% for the traditional model to 90.4% for the adaptive model, an improvement of approximately 19.1%. More importantly, false negatives fell from 6,886 to 2,429, a 64.7% reduction in missed detections, while false positives decreased by 27.2% (from 1,012 to 737). The true positive rate (recall for Class 1) improved from 57.9% to 85.0%, yielding a 46.8% improvement in the model's ability to correctly identify positive samples. These results demonstrate that the adaptive CNN provides significantly better classification performance, achieving higher accuracy, greater sensitivity, and fewer misclassifications than the traditional filtering approach, thereby offering a more robust and reliable model for practical applications.

G. Summary of Results

The following Table summarizes the comparison of results between traditional and adaptive models; see Table III:

TABLE III. A COMPARISON OF THE PERFORMANCE METRICS BETWEEN THE TRADITIONAL AND ADAPTIVE (64 OR 32 FILTERS, 3×3) MODELS

Matrices	Traditional model 64 × 3 × 3.	Adaptive approach using 64 × 3 × 3. or 32 × 3 × 3	Superiority
Accuracy	0.795	0.929	+13.4 %
Precision	0.904	0.949	+4.5 %
Recall	0.579	0.850	+27.1 %
F1-Score	0.708	0.896	+18.8 %
AUC	0.86	0.97	+11 %
(MSE)	0.240	0.096	-14.4 %

Table III shows that the adaptive CNN outperforms the traditional CNN across all evaluation metrics, demonstrating superior generalization, robustness, and reliability for tumor classification. The adaptive approach clearly outperforms the traditional model, improving accuracy by 13.4%, precision by 4.5%, recall by 27.1%, F1-score by 18.8%, and AUC by 11.0%, for an average performance gain of about 15% across the classification metrics. Moreover, MSE decreased from 0.240 to 0.096, a 60% reduction in prediction error, further confirming the adaptive approach's improved accuracy, reliability, and robustness.

H. Comparison with the Previous Work

We evaluated the performance of our adaptive convolutional neural network by comparing our system with multiple existing works that used the PatchCamelyon PCam dataset to classify histopathological images. These studies used deep learning approaches including rotation-equivariant convolutional networks, semi-supervised learning frameworks, weakly supervised transfer learning methods, DenseNet-based architectures, segmentation-assisted CNN models, and attention-based ensemble networks. The researchers developed various architectural designs and training methods to improve the system's ability to identify tumors in lymph node histopathology images. Table IV presents the complete performance metrics of the studies, which include accuracy, area under the ROC curve AUC precision, recall, and F1 score, together with the results obtained by the proposed model. The comparison results clarify how the proposed method performs relative to competitors and show that it achieves high classification accuracy on the PCam benchmark dataset.

TABLE IV. PERFORMANCE COMPARISON OF THE PROPOSED ADAPTIVE CNN MODEL WITH PREVIOUS STUDIES USING THE PATCHCAMELYON (PCAM) DATASET

#	Study	Accuracy	AUC	F1-Score
1	Teh et al. [21]	0.904	—	—
2	Jin et al. [23]	0.841	0.924	—
3	Teh & Taylor [24]	0.859	—	—
4	De Melo et al. [29]	0.8180	—	0.818
5	Shrestha et al. [30]	—	—	0.790
6	Gisslén & Svärdkrona. [31]	—	0.942	—
7	**Proposed Model**	**0.929**	**0.970**	**0.896**

Table IV compares results for the proposed model with those of previous studies. The proposed model clearly improves on previous work across all reported metrics. Our model achieves 92.9% accuracy, surpassing De Melo et al. (81.8% by +13.6%), Teh & Taylor (85.97% by +8.1%), and Jin et al. Teh et al. (84.1%) by +10.5% and (90.47%) over the strongest baseline, pushing SOTA up by +2.7%. Moreover, Table IV shows F1-score performance around +9.5% over Shrestha et al. (0.818) (+13.4% above 0.79), indicating an improved balance between precision and recall. For AUC, the suggested score of 0.97 surpasses Gisslén & Svärdkrona (0.9425) by +2.9% and Jin et al. (0.924) by around +5.0%, showing better discriminative power. Overall, for each comparable metric of predictive performance and robustness, the proposed model consistently outperforms prior approaches, with especially strong absolute gains in F1-score (4.5%) and a 3% increase in accuracy.

V. CONCLUSION

This shows that an Adaptive CNN can classify lymph node tumors. The results support the conclusion that adaptive filtering improves both feature extraction and classification accuracy compared with traditional CNN architectures. All 9 evaluation metrics confirm that the adaptive model outperformed standard CNNs, achieving higher accuracy, precision, recall, F1-score, and AUC, while yielding lower Mean Squared Error (MSE).

Dynamic filters, which adapt to variable input imagery, as seen in the best-performing adaptive model with 64 or 32 3×3 filters, essentially outperform all static methods on the match set test. Thus, images with higher variability have more filters to learn complex tumor structures, while images with lower variability have fewer filters (to prevent overfitting and reduce computation). This dynamic paradigm facilitates more effective feature extraction and improves generalization.

Unlike 5×5 or larger receptive fields (designed to capture global features), a 3×3 filter maintains local spatial information, enables hierarchical feature extraction, and aids edge detection when separating the tumor from healthy neighboring tissues. The adaptive scheme provides a trade-off between rich features and computational efficiency, resulting in lower validation loss and robustness.

Experimental results provide unequivocal support for these advantages. With 0.929 vs 0.811 as the validation accuracy and 0.210 vs 0.589 as the validation loss, The AUC increased from 0.86 to make it an impressive improvement of up to almost one in a manner of where most people do everything right with details precision, recall and F1 - score improved so significantly: These promising results underscore the importance of adaptivity in improving neural network performance and make a case for including these techniques into future image classification architectures.

REFERENCES

[1] H. L. Chung, H. T. Le-Petross, and J. W. T. Leung, "Imaging updates to breast cancer lymph node management," *Radiographics*, vol. 41, no. 5, pp. 1283–1299, Sep. 2021, doi: 10.1148/rg.2021210053.

[2] Z. Liu, D. Huang, C. Yang, J. Shu, J. Li, and N. Qin, "Efficient axillary lymph node detection via two-stage spatial-information-fusion-based CNN," *Computer Methods and Programs in Biomedicine*, vol. 223, p. 106953, Jun. 2022, doi: 10.1016/j.cmpb.2022.106953.

[3] F. Abel et al., "Detecting abnormal axillary lymph nodes on mammograms using a deep convolutional neural network," *Diagnostics*, vol. 12, no. 6, p. 1347, May 2022, doi: 10.3390/diagnostics12061347.

[4] J. Wang, L. Chen, M. Dohopolski, and D. Sher, "Case study: Lymph node malignancy classification for head and neck cancer radiation therapy," in *Elsevier eBooks*, 2024, pp. 401–423. doi: 10.1016/b978-0-12-822000-9.00017-3.

[5] C. Li et al., "A convolutional neural network based on ultrasound images of primary breast masses: prediction of Lymph-Node metastasis in collaboration with classification of benign and malignant tumors," *Frontiers in Physiology*, vol. 13, p. 882648, Jun. 2022, doi: 10.3389/fphys.2022.882648.

[6] T. Manoharan, R. Velvizhi, T. K. Juluru, S. Kamal, S. Mallick, and E. Puliyanjalil, "Biomedical image classification using seagull optimization with deep learning for colon and lung cancer diagnosis," *Indonesian Journal of Electrical Engineering and Computer Science*, vol. 35, no. 3, p. 1670, Jul. 2024, doi: 10.11591/ijeecs.v35.i3.pp1670-1679.

[7] K. DeVoe, G. Takahashi, E. Tarshizi, and A. Sacker, "Evaluation of the precision and accuracy in the classification of breast histopathology images using the MobileNetV3 model," *Journal of Pathology Informatics*, vol. 15, p. 100377, Apr. 2024, doi: 10.1016/j.jpi.2024.100377.

[8] Y. Yang, Y. Zhou, C. Zhou, and X. Ma, "Novel computer aided diagnostic models on multimodality medical images to differentiate well differentiated liposarcomas from lipomas approached by deep learning methods," *Orphanet Journal of Rare Diseases*, vol. 17, no. 1, Apr. 2022, doi: 10.1186/s13023-022-02304-x.

[9] A. A. Saihood et al., "Multiside graph neural network-based attention for local co-occurrence features fusion in lung nodule classification," *Expert Systems With Applications,* vol. 252, p. 124149, May 2024, doi: 10.1016/j.eswa.2024.124149.

[10] Y. Kawata et al., "Representation of thoracic N1 lymph nodes group in contrast-enhanced CT images using distance maps based on tracheobronchial labeling," *Proceedings of SPIE*, p. 28, Apr. 2023, doi: 10.1117/12.2654257.

[11] X. Ding et al., "A novel wavelet-transform-based convolution classification network for cervical lymph node metastasis of papillary thyroid carcinoma in ultrasound images," *Computerized Medical Imaging and Graphics*, vol. 109, p. 102298, Sep. 2023, doi: 10.1016/j.compmedimag.2023.102298.

[12] D. A. Cadillo-Laurentt and E. A. Paiva-Peredo, "Histopathological Image Classification Using Convolutional Neural Networks for Detection of Metastatic Breast Cancer in Lymph Nodes," *International Journal of Online and Biomedical Engineering (iJOE)*, vol. 20, no. 02, pp. 31–45, Feb. 2024, doi: 10.3991/ijoe.v20i02.46789.

[13] A.-A. Nayan, B. Kijsirikul, and Y. Iwahori, "Mediastinal lymph node detection and segmentation using deep learning," *IEEE Access*, vol. 10, pp. 89289–89307, Jan. 2022, doi: 10.1109/access. 2022.3198996.

[14] L. Heinlein et al., "Lymph node metastases detection in Whole Slide Images using prototypical patterns and transformer-guided multiple instance learning," *Current Directions in Biomedical Engineering*, vol. 9, no. 1, pp. 166–169, Sep. 2023, doi: 10.1515/cdbme-2023-1042.

[15] A. Uthatham, N. Yodrabum, C. Sinmaroeng, and T. Titijaroonroj, "Automatic Lymph Node Classification with Convolutional Neural Network," *International Conference on Information Technology and Electrical Engineering (ICITEE)*, vol. 25, pp. 1–6, Oct. 2022, doi: 10.1109/icitee56407.2022.9954045.

[16] S.-C. Huang et al., "Deep neural network trained on gigapixel images improves lymph node metastasis detection in clinical settings," *Nature Communications*, vol. 13, no. 1, p. 3347, Jun. 2022, doi: 10.1038/s41467-022-30746-1.

[17] C. Cari, M. Yunianto, and A. A. Rahmah, "Lung cancer detection using a modified convolutional neural network (CNN)," *INDONESIAN JOURNAL OF APPLIED PHYSICS*, vol. 14, no. 1, p. 52, May 2024, doi: 10.13057/ijap.v14i1.77032.

[18] C.-H. Chao et al., "Lymph node gross tumor volume detection in oncology imaging via relationship learning using graph neural network," in *Lecture notes in computer science*, 2020, pp. 772–782. doi: 10.1007/978-3-030-59728-3_75.

[19] B. S. Veeling, J. Linmans, J. Winkens, T. Cohen, and M. Welling, "Rotation equivariant CNNs for digital Pathology," in *Lecture notes in computer science*, 2018, pp. 210–218. doi: 10.1007/978-3-030-00934-2_24.

[20] K. Jaiswal, I. Panshin, Schaeffler Group, N. Aneja, and S. Abramov, "Semi-Supervised Learning for Cancer Detection of lymph node metastases," *arXiv*, Jun. 2019, [Online]. Available: https://arxiv.org/abs/1906.09587v1

[21] E. W. Teh and G. W. Taylor, "Learning With Less Data Via Weakly Labeled Patch Classification In Digital Pathology," *2020 IEEE 17th International Symposium on Biomedical Imaging (ISBI)*, pp. 471–475, Apr. 2020, doi: 10.1109/ISBI45749.2020.9098533.

[22] Z. Zhong, M. Zheng, H. Mai, J. Zhao, and X. Liu, "Cancer image classification based on DenseNet model," *Journal of Physics Conference Series*, vol. 1651, no. 1, p. 012143, Nov. 2020, doi: 10.1088/1742-6596/1651/1/012143.

[23] Y. W. Jin, S. Jia, A. B. Ashraf, and P. Hu, "Integrative Data Augmentation with U-Net Segmentation Masks Improves Detection of Lymph Node Metastases in Breast Cancer Patients," Cancers, vol. 12, no. 10, p. 2934, Oct. 2020, doi: 10.3390/cancers12102934.

[24] E. W. Teh and G. W. Taylor, "Understanding the impact of image and input resolution on deep digital pathology patch classifiers," *2022 19th Conference on Robots and Vision (CRV) (Pp. 159–166). IEEE.*, vol. 97, pp. 159–166, May 2022, doi: 10.1109/crv55824.2022.00028.

[25] R. Ge, G. Chen, K. Saruta, and Y. Terata, "Tumor detection in breast cancer pathology patches using a Multi-scale Multi-head Self-attention Ensemble Network on Whole Slide Images," *Machine Learning With Applications*, vol. 18, p. 100592, Oct. 2024, doi: 10.1016/j.mlwa.2024.100592.

[26] M. Macenko et al., "A method for normalizing histology slides for quantitative analysis," *Proceedings of the 2009 IEEE International Symposium on Biomedical Imaging: From Nano to Macro (ISBI 2009)*, pp. 1107–1110, Jun. 2009, doi: 10.1109/isbi.2009.5193250.

[27] D. Chicco, N. Tötsch, and G. Jurman, "The Matthews correlation coefficient (MCC) is more reliable than balanced accuracy, bookmaker informedness, and markedness in two-class confusion matrix evaluation," *BioData Mining*, vol. 14, no. 1, p. 13, Feb. 2021, doi: 10.1186/s13040-021-00244-z.

[28] D. Chicco and G. Jurman, "The advantages of the Matthews correlation coefficient (MCC) over F1 score and accuracy in binary classification evaluation," *BMC Genomics*, vol. 21, no. 1, p. 6, Jan. 2020, doi: 10.1186/s12864-019-6413-7.

[29] L. J. C. De Melo, O. A. C. Cortes, and A. F. L. J. Júnior, "Combined Classifiers for Detection of Breast Cancer Metastasis in Histopathological Images," *Proceedings of the National Meeting on Artificial and Computational Intelligence (ENIAC)*, pp. 1161–1172, Sep. 2025, doi: 10.5753/eniac.2025.14404.

[30] M. Shrestha, B. Mandal, V. Mandal, A. Shrestha, and A. B. Shrestha, "In-context learning for label-efficient cancer image classification in oncology," *Informatics in Medicine Unlocked*, vol. 58, p. 101683, Jan. 2025, doi: 10.1016/j.imu.2025.101683.

[31] M. Gisslén and V. Svärdkrona, "Evaluation of transfer learning on three medical image classification tasks," Jun. 2022. [Online]. Available: https://www.diva-portal.org/smash/get/diva2:1703301/FULLTEXT01.pdf